International Forum on Aeroelasticity and Structural Dynamics
IFASD 2017
25-28 June 2017 Como, Italy

# INFLUENCE OF GUST MODELLING ON FREE-FLIGHT AEROFOILS

**Reik Thormann**[1], **Giampaolo Pagliuca**[1], **Sebastian Timme**[1]

[1]School of Engineering
University of Liverpool
The Quadrangle, L69 3GH Liverpool, United Kingdom
reik.thormann@liverpool.ac.uk

**Keywords:** CFD, Resolved Gust, Field-Velocity Method, Flight Dynamics

**Abstract:** Gust analysis is one key task during design and certification of new aircraft. In the industrial standard, the gust is modelled as a disturbance in velocity and is superposed with the general velocity field surrounding the aircraft. The shape, typically sinusoidal or 1-cos, is uniform in vertical direction and is not changing while travelling through the computational domain. These assumptions known as the field or disturbance velocity method facilitate an efficient way of simulating gust encounter within computational fluid dynamics methods. However, how this frozen gust model effects the accuracy of loads predictions compared to more-realistic models remains an open question. A novel approach to simulate a so-called resolved gust is presented herein. An initial perturbation of the x-velocity is prescribed using a 1-cos shape in two spatial directions. Disturbances in vertical velocity as well as density and pressure are developing after some simulated time. Results are compared to the field-velocity method using the CRANK aerofoil covering subsonic and transonic flow conditions. Lift and moment responses are analysed as well as time histories of velocities at different grid locations. Furthermore, a second aerofoil is added as a horizontal tail-plane to represent a large civil aircraft. This configuration is used to include the effects of flight dynamics while analysing the responses due to the two gust models.

## 1 INTRODUCTION

In the industrial standard, the gust is modelled as a disturbance velocity and is superposed with the general velocity field surrounding the aircraft. The shape, typically sinusoidal or 1-cos, is constant with respect to altitude and is not changing while travelling through the computational domain. These assumptions are no restrictions for methods based on linear potential theory such as the doublet-lattice method [1], since these methods cannot capture the interaction between lifting surfaces and the gust as well as a coupling of the different flow quantities e.g. between velocity and density.

After introducing the field velocity method (FVM) within computational fluid dynamics [2] including industrial configurations [3, 4], a question regarding the influence of the above assumptions comes into focus. A comparison to a so-called resolved approach was presented in [5]. The gust, which is constant in vertical direction, is introduced at the far-field boundary using a Reynolds-averaged Navier-Stokes (RANS) method of second order in space. Overset grids are applied in order to reduce the overall grid size. While the gust is still a disturbance in the velocity field only, the interaction of the gust with the aircraft is covered and quantified.

Differences for a two-dimensional wing with horizontal tail-plane configuration could only be observed for a 1-cos gust with a wave length shorter than two reference chords. A split-velocity method [6, 7] was introduced as a novel gust model. In this approach source terms capture the effect of bodies onto the gust. Differences to the common FVM could only be observed for the shortest gust lengths as well.

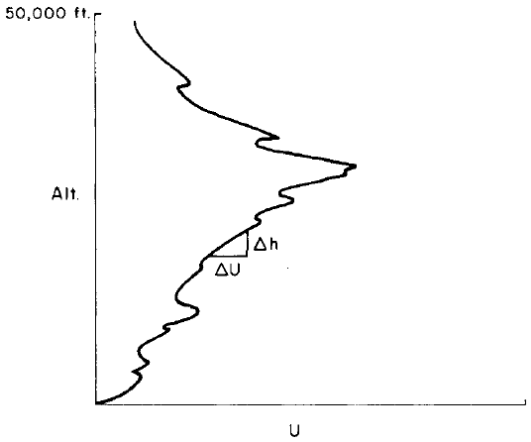


Figure 1: Wind gradient by Houbolt [8]

All preceding papers prescribed a vertical disturbance velocity. However, a gust at cruise conditions is usually caused by a gradient in horizontal velocity with respect to altitude [8], shown in Figure 1. Consequently, the gust is not constant with respect to altitude which could influence the interaction between the body and the gust. Moreover, disturbances in all flow variables are introduced including density and pressure which might affect the aerodynamic loads.

In this paper, a second order RANS code is used to compare results of a resolved gust approach with the standard FVM for an aerofoil case. The resolved gust is simulated using a background grid with a Cartesian block in the relevant grid region to avoid a dissipation of the gust. The gust itself is prescribed as a change in horizontal velocity using a 1-cos function in both spatial dimensions. This disturbance is introduced into the RANS code by altering a restart file. The background grid is merged with the near-field grid of the CRANK aerofoil. Results are presented comparing global lift and moment coefficient as well as the velocity at different points within the flow field. In a second test case, a NACA 0008 aerofoil is added to the CRANK aerofoil to describe a horizontal tail-plane (HTP) representative of a large civil aircraft. Results are discussed for the rigid as well as for a free-flying configuration considering both translational and the rotational degrees of freedom.

## 2 NUMERICAL APPROACH

### 2.1 Computational Fluid Dynamics Solver

All simulations are performed with an in-house, semi-meshless Navier-Stokes flow solver [9,10] coupled with the Spalart-Allmaras turbulence model [11]. Convective fluxes are discretised using upwind schemes, specifically the Osher solver for the mean flow equations [12]. A weighted least squares procedure calculates the gradients of the flow variables, required for viscous fluxes as well as source terms in the turbulence model. The steady-state solution is obtained applying a fully implicit backward Euler method with local time-stepping, while additionally a second-order dual-time stepping is utilised in unsteady time-marching simulations. Linear equations arising from the implicit time integration are solved throughout using a restarted generalised

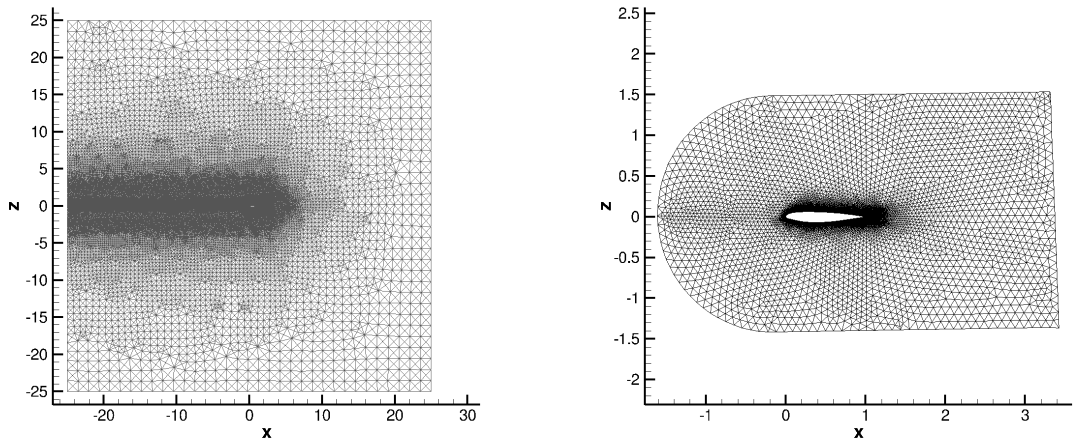


(a) Background grid

(b) Near-field grid of CRANK aerofoil

Figure 2: Point cloud and stencils of computational grids

conjugate residual method preconditioned with an incomplete lower-upper factorisation [13]. A no-slip boundary condition is used at solid walls, while non-reflecting boundary condition of Whitfield and Janos [14] is applied at the far-field boundary.

### 2.2 Resolved Gust Simulations

A background grid with a Cartesian block is used to avoid the dissipation of the disturbance velocities. The remaining computational domain is discretised by unstructured quadrilaterals, see Figure 2(a). The background grid is merged with the near-field grid of the CRANK aerofoil, shown in Figure 2(b). This approach is used in order to retain the low dissipation property of the Cartesian grid block while resolving the boundary layer as well as local flow features around the aerofoil. Since a semi-meshless solver is used, a grid consist only of a cloud of points and a connectivity list of neighbouring points. Thus, a merging of grids involves an updating of the connectivity list and points within the solid walls must be removed. Additional points are removed close to the surface to protect the first layers of the boundary grid. The resulting grid comprises about $250\,000$ points and is presented in Figure 3. The new connectivity is obtained by interpreting the stencils as elements. A look-up is performed to find interior points per element, which become candidates for the new stencil. An angle and distance criterion is applied to retain compact stencils. Finally, the commutative property of the stencils is enforced; if point $P$ is in the stencil of point $R$, then also point $R$ is a stencil point of $P$.

After the new grid is obtained, a steady-state flow field is computed and the restart file is altered. A 1-cos with wave length $\lambda$ in both spatial dimensions is prescribed, see Figure 4(a):

$$u(t=0) = u_{\text{steady}} + u_g$$

$$u_g = \frac{\hat{u}}{2}\left[1 - \cos\left(2\pi\frac{x - x_0}{\lambda}\right)\right]\left[1 - \cos\left(2\pi\frac{z - z_0}{\lambda}\right)\right],$$

with $(x_0, z_0)$ denoting the location of the maximum and $\hat{u}$ the amplitude, which is set to $5\,\%$ of the free-stream velocity. Just the x-velocity component is perturbed, while all other flow variables remain at their steady values. The 1-cos shape is selected, because it is commonly used

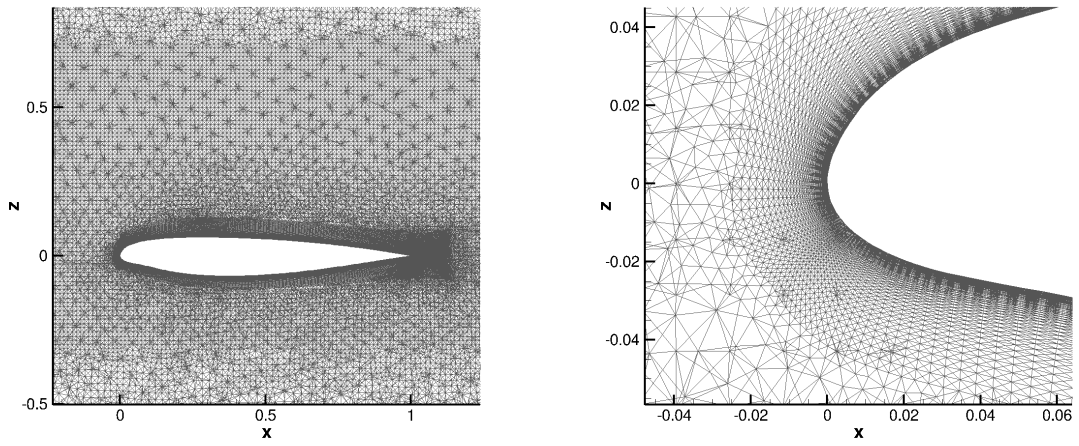


(a) overview (b) zoomed in at the nose

Figure 3: Merged grid

in gust analysis. Moreover, it simplifies the simulation process compared to a sharp-edged gust where a modified inflow boundary condition has to be implemented to retain the gust velocity at the boundary during the convection of the gust. The disturbance is imposed significantly upstream of the aerofoil to allow the gust to develop before encountering the aerofoil. A distance to the far-field boundary is retained to avoid a strong influence of reflections. At each maximum or minimum of the gradient, a vertical flux originates resulting primarily in a change in z-velocity, shown in Figure 4(c). The vertical position of the initial disturbance is chosen so that the maximum of the developed z-velocities will hit the aerofoil. Moreover, a change in density is obtained. Since the disturbance velocity is introduced instantaneously, a sound wave is generated travelling with sonic speed plus or minus the convective speed, respectively. This sound is a factor of ten larger than the obtained density disturbance moving with the convective speed and can be observed at the borders of Figure 4(d).

### 2.3 Extracting Disturbance Velocities for FVM

The resulting gust velocities of the resolved gust described above are used to perform a second gust simulation using FVM. After subtracting the steady flow filed, a least-square fit of the disturbance velocities is calculated to obtain an analytic expression which can be used more easily within an unstructured RANS code. The curve fit is only performed within a window including the gust velocities. The coordinates are normalised to $[0, 1] \times [0, 1]$. A combination of sine and cosine functions are used in each spatial dimension as well as linear and bi-linear polynomials

$$V_g^{\text{FVM}} = A + Bx + Cz + Dxz + \\ + \left( \sum_{i=0}^{N} E_i \cos(i\omega x) + F_i \sin(i\omega x) \right) \left( \sum_{j=0}^{N} G_j \cos(j\omega z) + H_j \sin(j\omega z) \right).$$

The coefficients are calculated at a time step, when the gust is fully developed but still upstream of the aerofoil.

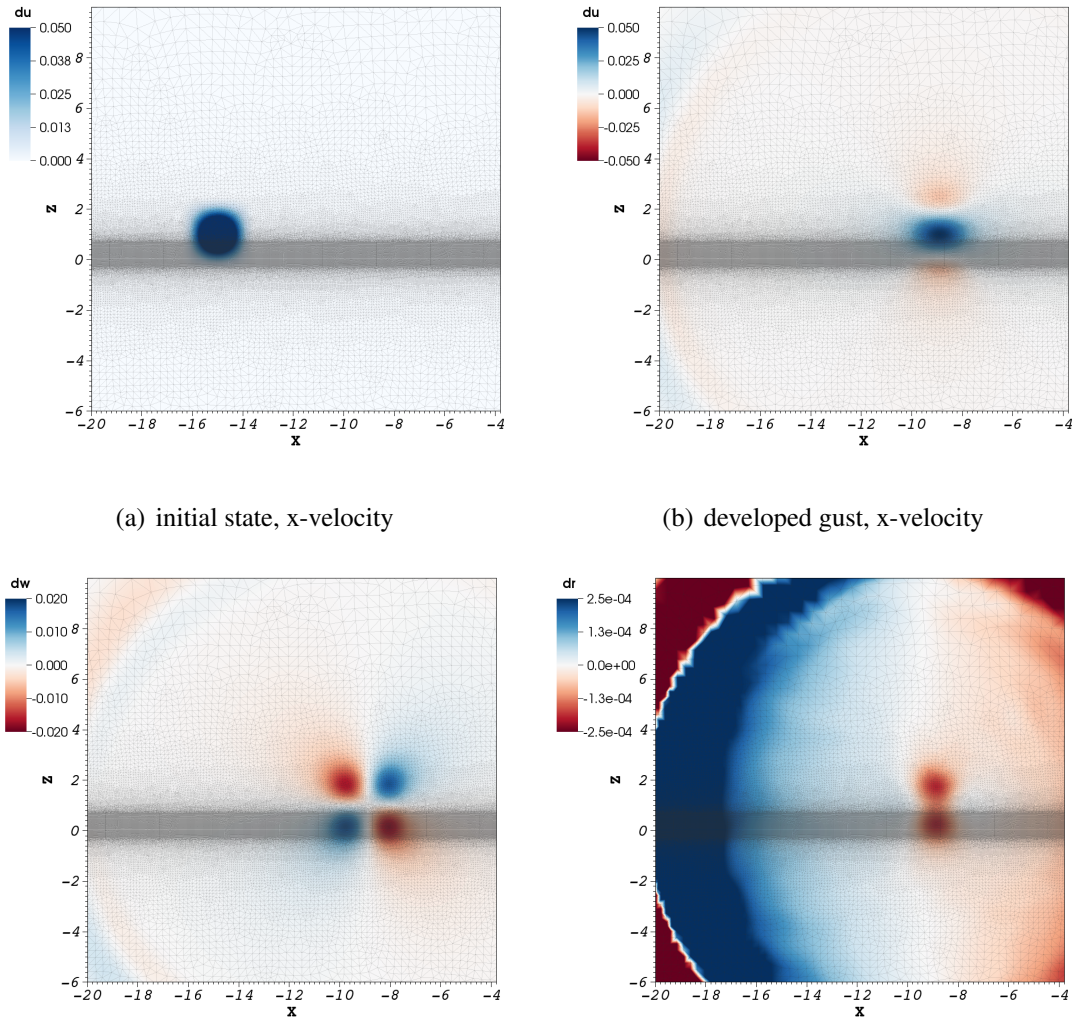


(a) initial state, x-velocity

(b) developed gust, x-velocity

(c) developed gust, z-velocity

(d) developed gust, density

Figure 4: Disturbance in x- and z-velocity components as well as in density

In Figures 5(a) and 5(c) the approximated gust velocities in x- and z-direction are presented, while Figures 5(b) and 5(d) show the corresponding error normalised by the maximum gust velocity. The approximation was obtained using $N = 15$ frequencies and a wave length $\lambda$ of three chords for the initial disturbance in the resolved approach. The colour bar for the error contour plot is scaled to a maximum of $1\,\%$ of the excitation amplitude which corresponds to $0.05\,\%$ of the free-stream velocity. Deviations mainly occur at the border of the window, where the values are small anyway, but stay below the $1\,\%$ error margin. Increasing the number of frequencies and thus the number of coefficients in the approximation naturally decreases the error further. However no impact on the computations was observed.

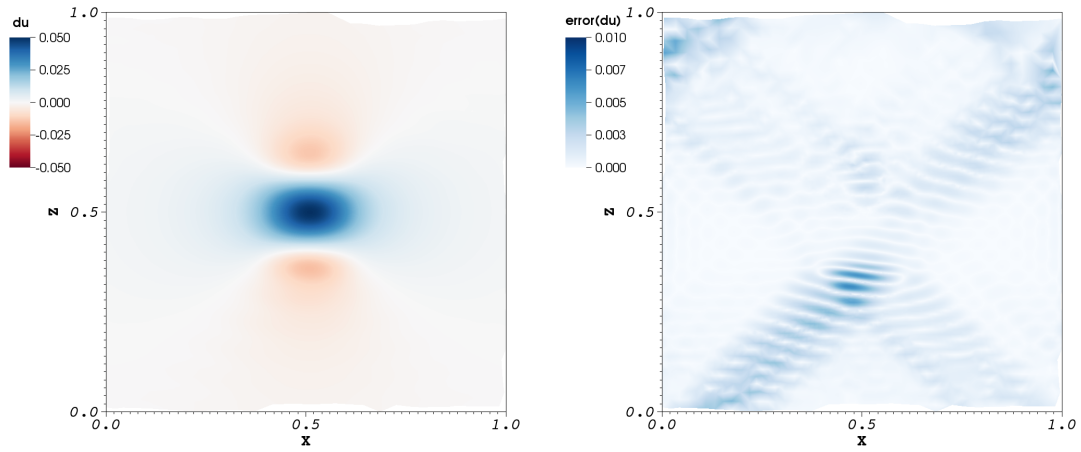


(a) x-velocity FVM

(b) x-velocity error

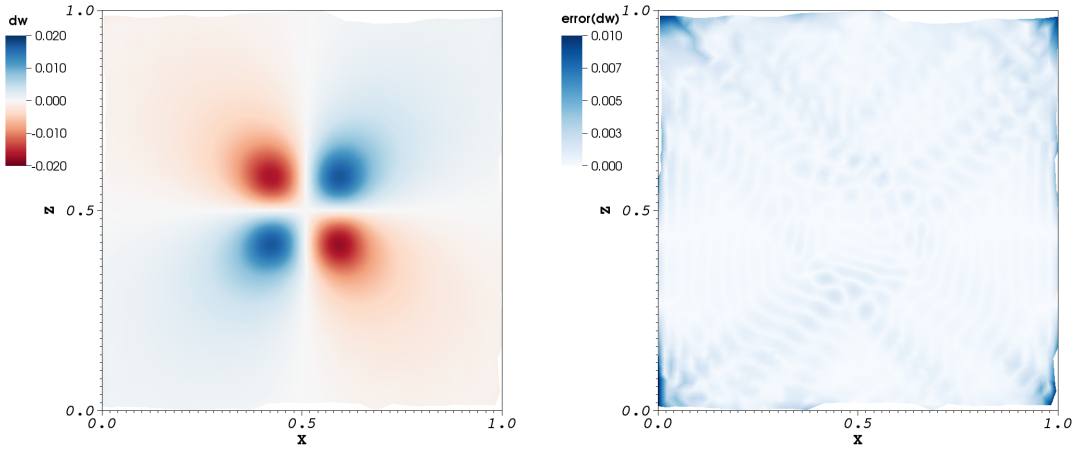


(c) z-velocity FVM

(d) z-velocity error

Figure 5: Approximation of gust velocities and its relative error with respect to the excitation amplitude for $N = 15$ and $\lambda = 3c$

## 3 SINGLE-AEROFOIL RESULTS

Three different test cases are analysed using the CRANK aerofoil. Two different wave lengths of 3 and 15 chords are simulated at a subsonic Mach number of 0.5. The shorter wave length is also simulated at transonic flow conditions using a Mach number of 0.754. The Reynolds number is kept constant throughout at seven million based on the chord length. The contour of the steady pressure coefficients is shown in Figure 6 for both flow conditions. In Figure 6(a) the stagnation pressure and suction peak can be observed while the contour plot in Figure 6(b) exhibits re-compression shocks on both sides of the aerofoil.

In the first test case, a gust of 3 chord lengths is simulated at subsonic flow conditions. The disturbance in x-velocity is introduced 25 chord lengths upstream of the aerofoil. In Figure 9, the lift and moment coefficients computed with the resolved approach are compared to two different FVM computations either using only the z-velocity component of the gust or the full velocity vector. The large influence of the gust's x-velocity is already obvious in the lift response. Neglecting this effect reduces the amplitude by about 40 %. The amplitude effect is smaller in the moment coefficient, however a different time progression is predicted. Using the

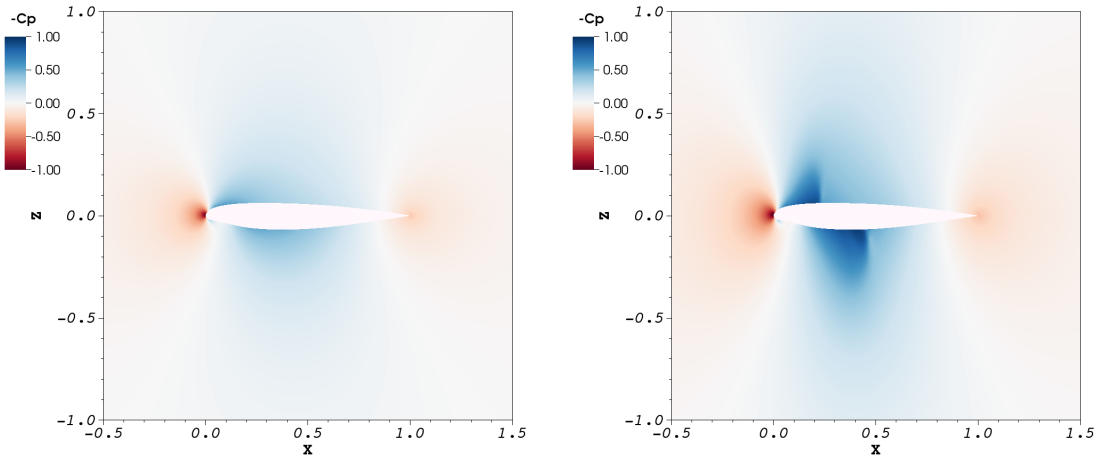


(a) Mach = 0.5 (b) Mach = 0.754

Figure 6: Steady pressure contours for CRANK aerofoil

full disturbance-velocity vector results in an excellent agreement with the resolved approach considering the lift coefficient. A fair agreement is also obtained for the moment coefficient while deviations can be observed at the peak values. While the minimum is under-predicted by the FVM, a higher maximum value is computed. The change in lift and moment around a non-dimensional time of four in the resolved approach is caused by the sound wave which is passing the aerofoil.

The gust-induced unsteady velocities are presented in Figures 9(c) and 9(d) at different streamwise grid positions. The initial peaks, which are more pronounced in the x-velocity, are the sound wave passing the observed grid point. However, the focus is on the perturbations moving with convective speed. The x-velocity exhibits two maxima and a minimum in-between, while a minimum followed by a maximum can be observed for the z-velocity. The velocities at $10$ and $5$ chord lengths upstream of the aerofoil agree well. This demonstrates a developed gust as well as the low dissipation on the grid preserving the gust shape over five travelled chord lengths. The shape is unchanged close to the lifting body, but its magnitude is decreased. Focusing on a point located half a chord length downstream of the aerofoil, the shape and amplitude has changed. These deviations can either be the result of the gust on the velocity field or a change of the gust shape due to the lifting surface. If the gust is the source of these differences, they should be also predicted using the FVM. In this case, the difference in velocity between the resolved and the FVM approach should be the gust itself independent from the grid position. The comparison is presented in Figures 9(e) and 9(f). Half a chord upstream of the aerofoil, the gust shape is unchanged compared to the reference at five chords in front of the aerofoil. A small deviation can be observed half a chord behind the aerofoil. The magnitude is slightly decreased in both velocity components. Thus, the influence of the aerofoil on the gust is small explaining the good agreement between FVM and the resolved approach regarding the global loads, which confirms previous work [5]

Also in [5], an improved prediction quality of the FVM is reported with increasing gust length. Thus, a medium gust length of $15$ chords is analysed at the same subsonic flow conditions. The response in lift and moment coefficients are shown in Figures 10(a) and 10(b), respectively. Compared to the shorter gust length, the amplitude of the lift response is nearly doubled while the response in moment in halved. An excellent agreement is obtained in the lift response be-

tween the resolved approach and its FVM counterpart, while deviations remain at the minimum and maximum of the moment coefficient. Results of the FVM using only the z-component of the disturbance velocity vector are not analysed, since large deviations are already observed for the shorter gust velocity.

Comparing the unsteady velocities at different grid locations, see Figures 10(c) and 10(d), the profile remains unchanged between $20$ and $10$ chord lengths upstream of the aerofoil. Closer to the surface, the amplitude of the z-velocity is increased in front and decreased behind the aerofoil. On the other hand, the unsteady x-velocity component does not change half a chord upstream. However, the shape is altered after passing the body showing a more pronounced minimum. The velocities predicted by the resolved and the field-velocity method are depicted in Figures 10(e) and 10(f). The x-velocity in front of the aerofoil is agreeing well with its reference $10$ chords upstream, while an increased amplitude in z-velocity can be observed. However, this not necessarily indicates that the gust shape is already altered due to the lifting surface, since the lift responses agree well. It could be explained by the difference in the surface boundary condition. In the resolved method, the velocity is zero at the boundary, while in the FVM the surface velocity is set to the gust velocity, since they are imposed as grid velocities. A change in the gust shape can be seen downstream of the aerofoil. The amplitude of the z-velocity is slightly reduced and a small phase difference can be observed. In the x-velocity the minimum is altered as well as the second maximum.

In summary, results computed with the resolved approach agree excellently in the lift coefficient for both gust lengths. Small deviations can be observed in the moment coefficient, however the absolute values are smaller for the longer gust length. These differences can not justify the additional computational cost of a resolved gust simulation involving a significantly finer mesh sizes and finer time-step sizes.

Subsequently, the Mach number is increased to $0.754$ in order to analyse both methods at transonic flow conditions, which includes an additional interaction between the gust and the recompression shock. Since a minor influence of the gust length was observed for the subsonic case, only the shorter gust length is analysed. Comparing the lift response in Figure 11(a) an excellent agreement is obtained as for the other test cases. The induced moment coefficient predicted by FVM deviates slightly in the minimum as well as in the maximum thereafter.

While the z-velocities at $10$ and $5$ chord lengths upstream of the aerofoil agree well, see Figure 11(d), a deviation in the first maximum of the x-velocity can be observed in Figure 11(c). The difference in z-velocity between the resolved and the field-velocity method shown in Figure 11(f) is almost independent from the position in the grid. Only a small deviation can be seen in the minimum for the position half a chord length downstream of the aerofoil. Small differences between the three different grid points can be seen in the x-velocity presented in Figure 11(e).

## 4 RESULTS OF WING-TAIL CONFIGURATION

In a second configuration, the geometric complexity and physical realism are increased by adding a NACA 0008 aerofoil representing a HTP. The second aerofoil is located $2.5$ reference chords behind and $0.25$ reference chords above the first aerofoil. The grid-merging technique as described in Section 2.2 is applied to obtain the new discretisation of the computational domain comprising $290\,000$ points. This configuration is analysed at the same transonic flow conditions as for the single aerofoil in the previous section using a Mach number of $0.75$.

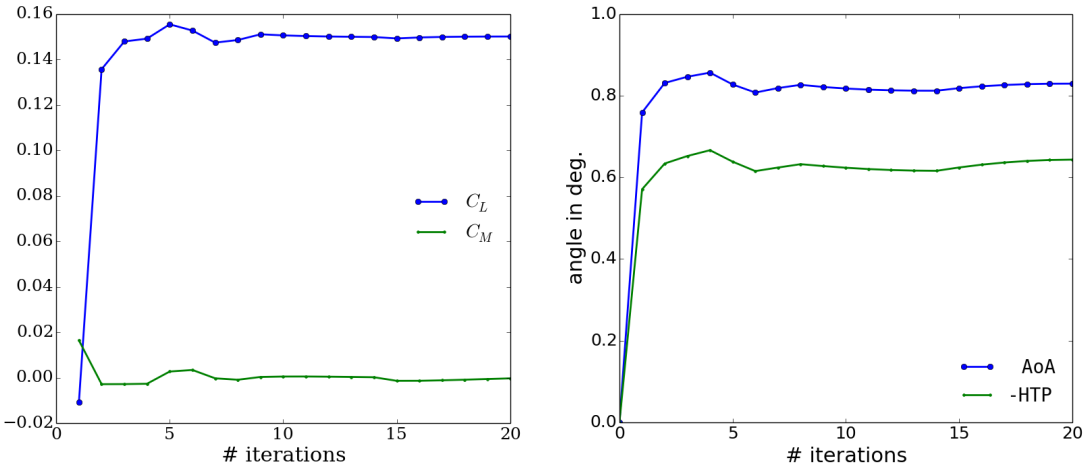


(a) Convergence of coefficients (b) Convergence of angles

Figure 7: Convergence history of the trimming procedure

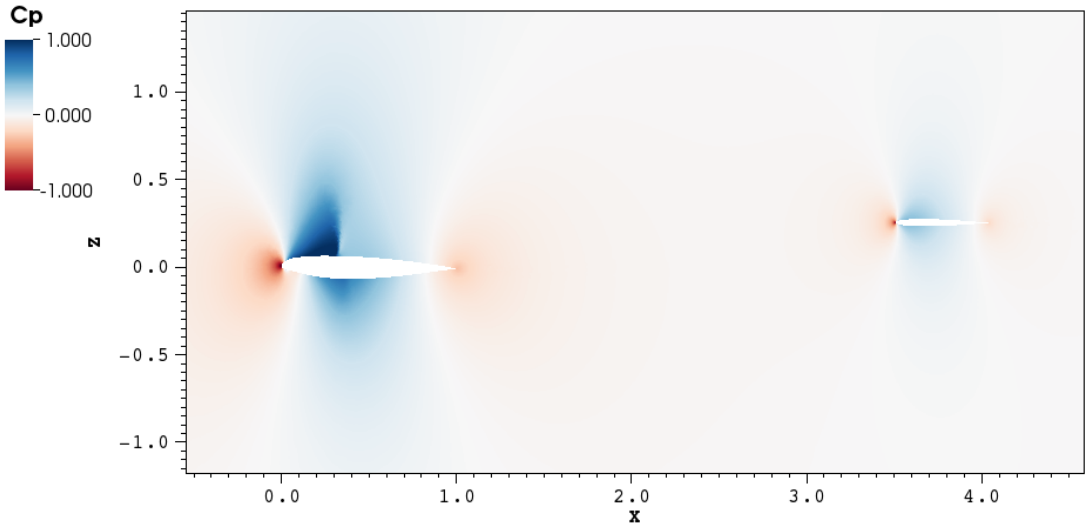


Figure 8: Steady pressure coefficient for wing-HTP configuration

In a first step, the static equilibrium is computed for the coupled system of aerodynamic and flight dynamic degrees of freedom applying Broyden method [15]. Target values of lift and moment coefficients of $0.15$ and $0.0$, respectively, are chosen based on representative level flight conditions. At each trimming iteration, tail rotation is imposed with mesh deformation using Radial basis functions [16]. Loads are calculated with few iterations of a steady-state computation. Thrust balances the drag at equilibrium condition. The target lift and moment coefficient are reached after $20$ iterations. The progression of the angle of attack and the deflection angle of the horizontal tail plane are presented in Figure 7(b). Starting at an initial condition of zero degree, the trimming variables converge as damped oscillation to their final values of $0.83$ deg for the angle of attack and $-0.64$ deg for the HTP. The resulting steady pressure coefficients are presented as a contour plot in Figure 8. The flow around the CRANK aerofoil is transonic exhibiting a re-compression shock on the upper surface. As a result of the trimming loop, the shock on the lower surface, which is present in Figure 6(b) for the single aerofoil at zero degree incidence nearly vanished. The flow remains subsonic at the thin HTP-aerofoil.

Before analysing the response of the fluid-flight dynamics coupled system due to a gust encounter, results of the static configuration are discussed first. In Figure 12, the gust response of the resolved approach is compared to its field-velocity counterpart. The gust velocities are extracted from the resolved simulations as discussed above. In addition, a second field-velocity simulation was conducted in which the gust velocities are extracted at $z = \text{const} = 0$. This profile is extruded uniformly along the z-axis. Results obtained by the field-velocity approaches are denoted "FVM 2D and "FVM 1D" respectively.

The response in lift coefficient presented in Figure 12(a) exhibits a minimum and two maxima. The first minimum and maximum are caused by the gust passing the first aerofoil while the last maximum is related to the gust response of the HTP. Similar to the single-aerofoil case, see Figure 11(b), a minimum followed by a maximum can be observed in the moment coefficient. An excellent agreement including the extrema is obtained between the resolved approach and FVM 2D. Only small deviations can be observed at the second maximum of the lift response. While the agreement with results computed by FVM 1D fair in the moment coefficient, larger differences can be seen in the lift response, especially at the two maxima. When analysing the lift response of wing and HTP individually as shown in Figures 12(c) and 12(d), the wing predominantly contributes to these deviations. Differences can be seen at the HTP, however their absolute values are smaller compared to the wing. The good agreement between the resolved approach and FVM 2D is also shown in Figures 12(e) and 12(f). If the assumption of a constant gust shape within the FVM is valid, the present difference in z-velocity between both methods should be the gust disturbance velocities independent from the investigated time step. After $8$ simulated travelled chords the gust is fully developed and this time-step is used as starting point for the corresponding FVM simulation while small perturbations of sound waves are omitted. At a non-dimensional time of $16$ the first half of the gust passed the first aerofoil. Nevertheless, an excellent agreement between the gust shape in Figures 12(e) and 12(f) is obtained. Passing the first aerofoil had a negligible effect on the gust velocities which supports the assumptions within the FVM.

In the final test case, the response of the fluid-flight dynamics coupled system is presented. At each inner iteration of the dual-time stepping scheme, position and velocity of the centre of gravity are updated by integrating the equations of motion [17] including aerodynamic forces from the RANS solver as well as body forces such as gravity. Radial basis function interpolation [16] is applied to move the grid points accordingly whereas grid point velocities are calculated with finite differences. In particular, the configuration investigated here is representative of the longitudinal dynamics of a large civil aircraft flying at $10\,\text{km}$ altitude. For two-dimensional longitudinal problems, flight dynamics is described with $6$ unknowns. The horizontal and vertical translations are referred to inertial axes [18]. The rigid rotation is the Euler angle describing the orientation of the body relative to the inertial reference frame. The rotation point coincides with the centre of gravity at $10\,\%$ of wing chord. The horizontal and vertical velocities in the body reference frame are assumed variations from the corresponding velocities at equilibrium condition. The properties of the system are expressed by means of non-dimensional quantities by defining the reference length as half a wing chord length. The non-dimensional radius of gyration is set to $1.5$ and the mass ratio to $73$.

In Figures 13(a) and 13(b), a qualitatively similar lift and moment responses are obtained as for the static simulation. Overall, a good agreement between the resolved approach and the FVM is obtained while deviations can be observed at the second maximum of the lift response. When analysing the lift response for wing and tail separately, differences can be observed at the first

aerofoil as shown in Figure 13(c) while only minor deviations can be seen on the HTP shown in Figure 13(d). The response of the flight-dynamics degrees of freedom is presented in Figures 13(e) and 13(f) for the z-velocity of the centre of gravity and the pitch angle, respectively. Larger deviations can be observed in the z-velocity after a non-dimensional time of $15$. A similar trend is computed for the pitch angle but a lower maximum is predicted by the FVM. However, when comparing to the steady angle of attack of $0.83$ deg the difference in the pitch-angle response between the two methods is one order of magnitude smaller.

## 5 CONCLUSION AND OUTLOOK

A novel approach is presented to simulate a gust without assuming a constant shape with respect to altitude and over time. The method also includes the coupling of the different flow quantities as well as the bi-directional interaction of the gust and the body. Instead of directly prescribing a disturbance in z-velocities uniformly in vertical direction, a 1-cos shape of x-velocity is used in both spatial directions. After progressing in time, a disturbance in the z-velocity develops as well as in density and pressure. A background grid comprising a Cartesian block is used to avoid a dissipation of the gust velocities. This grid is merged with a near-field grid of the CRANK aerofoil. In a second configuration, a NACA 0008 aerofoil was added as horizontal tail-plane representing a large civil aircraft.

Results are compared to the commonly applied field-velocity method at subsonic and transonic flow conditions using two different gust lengths. An excellent agreement in the gust-induced lift coefficient is obtained throughout. Overall, the response in moment coefficient is agreeing well, while small deviations can be observed at the peak values. The obtained disturbances in density and pressure are small and have a negligible influence on the global coefficients. The quality of the grid could be approved, when analysing the unsteady velocities at different grid locations. Moreover, only a minor change of the gust shape due to the lifting surface is observed for all presented test cases. Similar results are obtained for the wing-tail configuration showing a good agreement in the lift response of the individual aerofoils. Minor deviations are observed in the flight-dynamic response due to the gust encounter. However, the differences are one orders of magnitude smaller compared to the values obtained from the steady trimming procedure.

In summary, the field-velocity method is able to accurately predict the unsteady loads for the considered test cases, while being computational more efficient. It is two to three times faster on the same grid than the resolved approach, since more inner iterations in the dual-time stepping scheme are required to reach the residual-based convergence criterion while the gust develops. Moreover, significantly coarser grids can be used if the field-velocity method is applied. The gust is prescribed throughout the simulation and thus cannot dissipate. Hence, the increased computational cost of resolving the gust does not seem to be justified.

## ACKNOWLEDGEMENT

The research leading to this work was supported by the AEROGUST project, which has received funding from the European Commission under grant agreement number 636053. The partners in AEROGUST are: University of Bristol, INRIA, NLR, DLR, University of Cape Town, NUMECA, Optimad Engineering S.r.l., University of Liverpool, Airbus Defence and Space, Dassault Aviation, Piaggio Aerospace and Valeol.

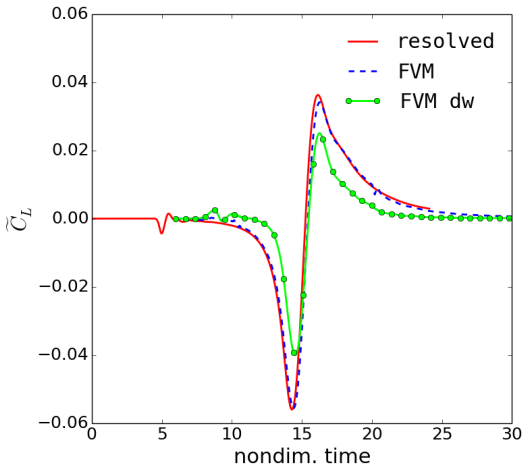


(a) disturbance lift coefficient $\widetilde{C}_L$

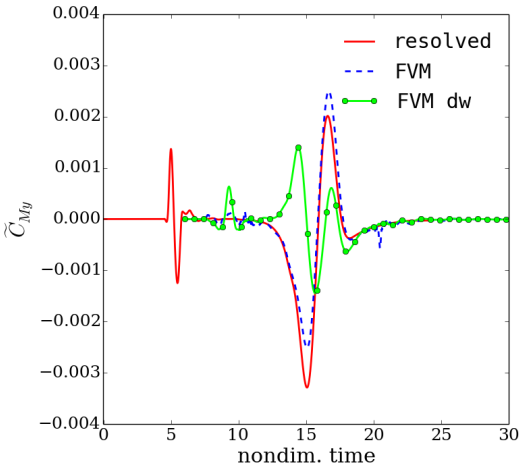


(b) disturbance moment coefficient $\widetilde{C}_M$

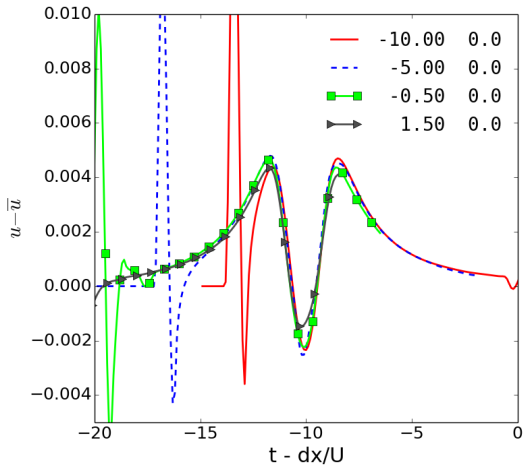


(c) x-velocity, difference to steady state $\bar{u}$, resolved approach

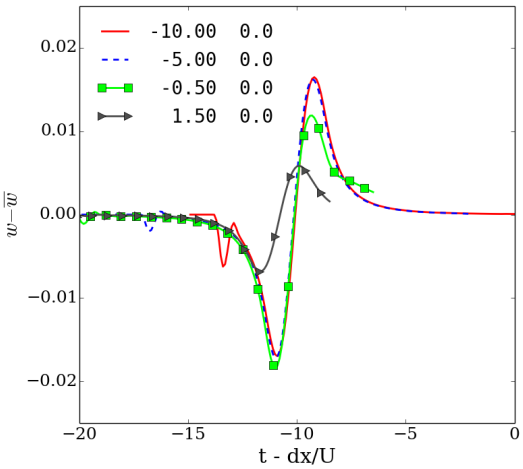


(d) z-velocity, difference to steady state $\bar{w}$, resolved approach

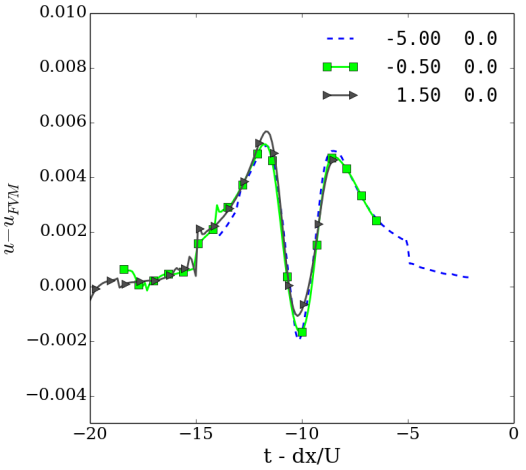


(e) x-velocity, difference to FVM

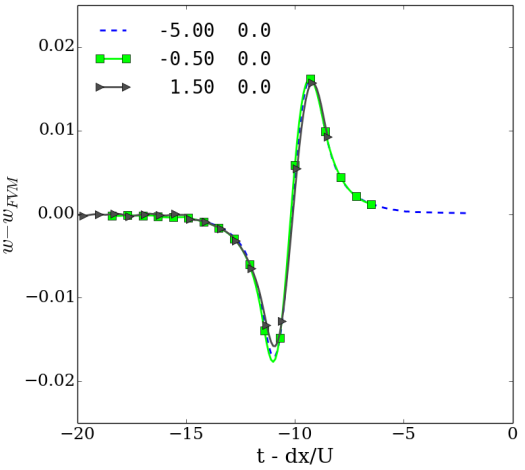


(f) z-velocity, difference to FVM

Figure 9: Comparison of gust induced lift and moment coefficient as well as velocities at different grid locations for $\lambda = 3c$ and Mach = 0.5

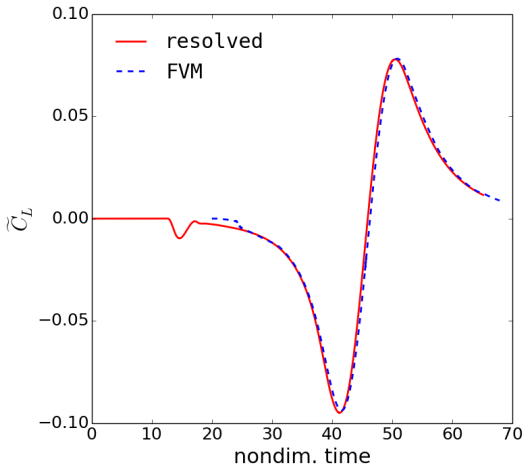


(a) disturbance lift coefficient $\widetilde{C}_L$

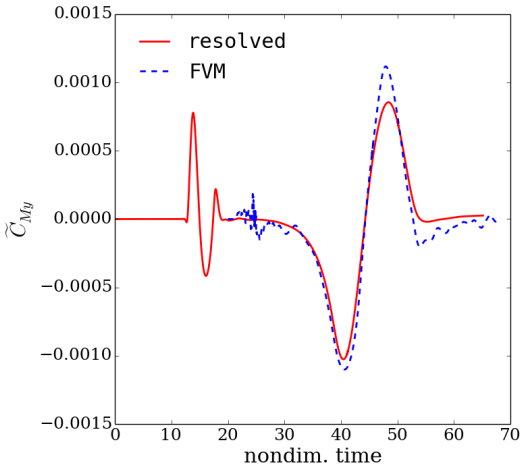


(b) disturbance moment coefficient $\widetilde{C}_M$

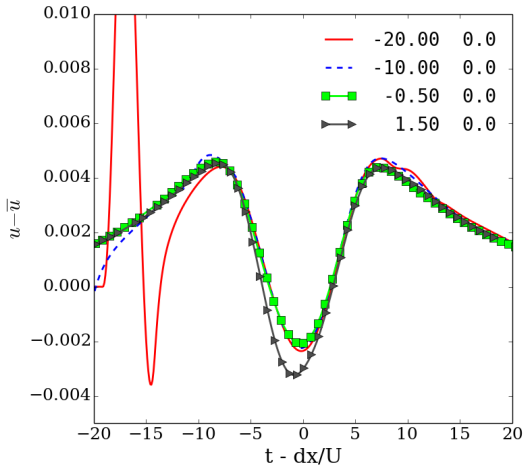


(c) x-velocity, difference to steady state $\bar{u}$, resolved approach

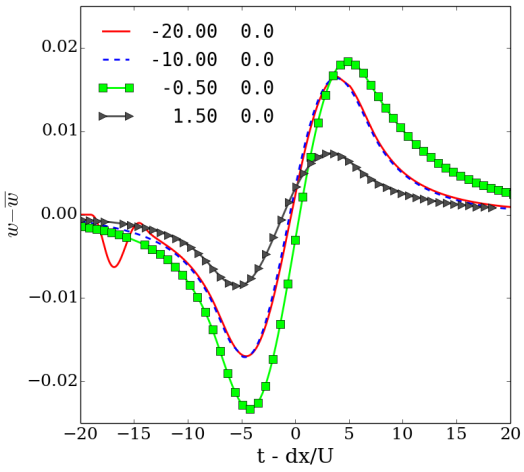


(d) z-velocity, difference to steady state $\bar{w}$, resolved approach

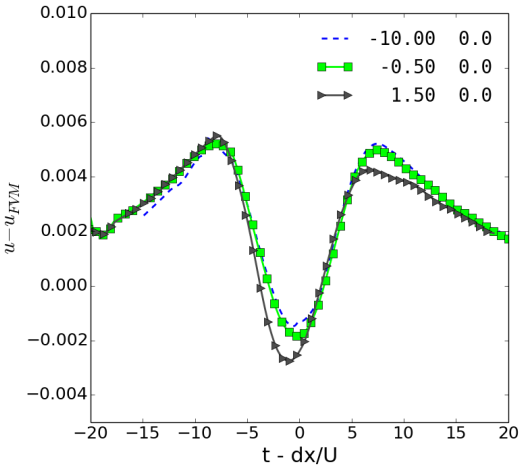


(e) x-velocity, difference to FVM

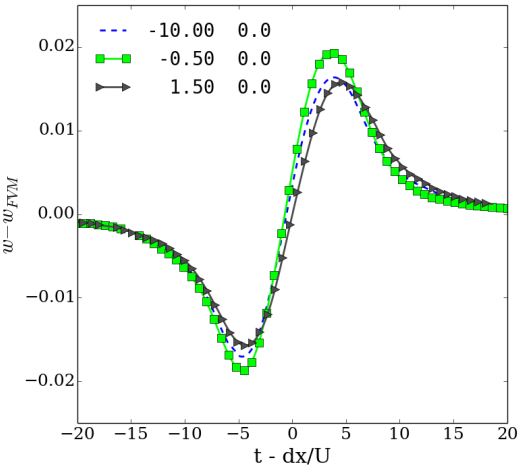


(f) z-velocity, difference to FVM

Figure 10: Comparison of gust induced lift and moment coefficients as well as velocities at different grid locations for $\lambda = 15c$ and Mach = $0.5$

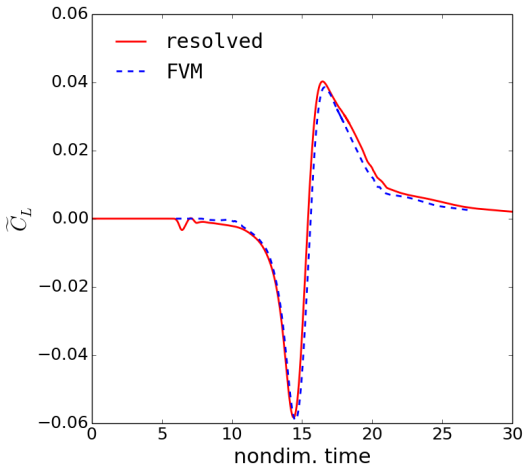


(a) disturbance lift coefficient $\widetilde{C}_L$

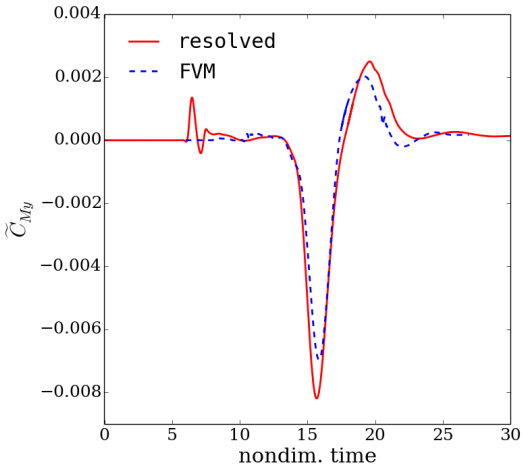


(b) disturbance moment coefficient $\widetilde{C}_M$

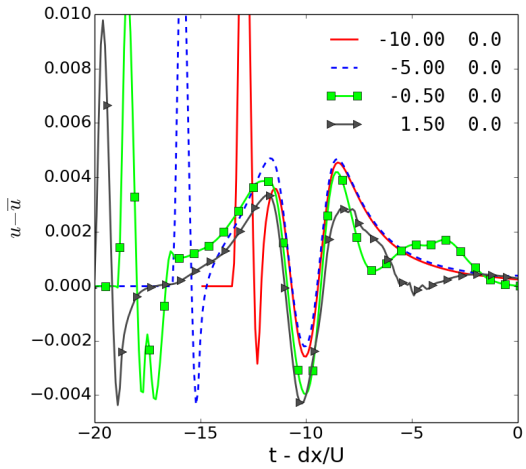


(c) x-velocity, difference to steady state $\bar{u}$, resolved approach

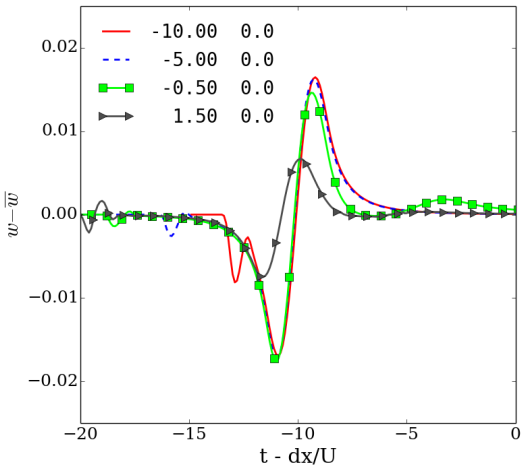


(d) z-velocity, difference to steady state $\bar{w}$, resolved approach

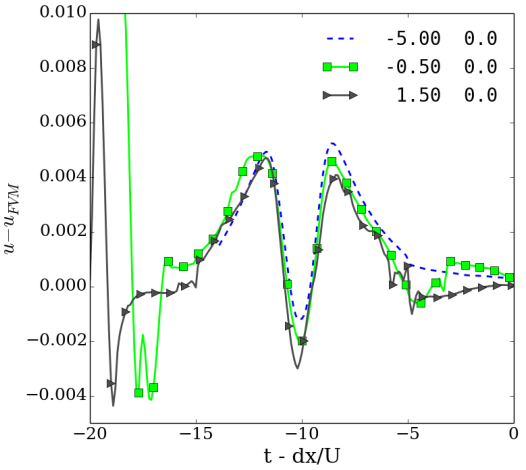


(e) x-velocity, difference to FVM

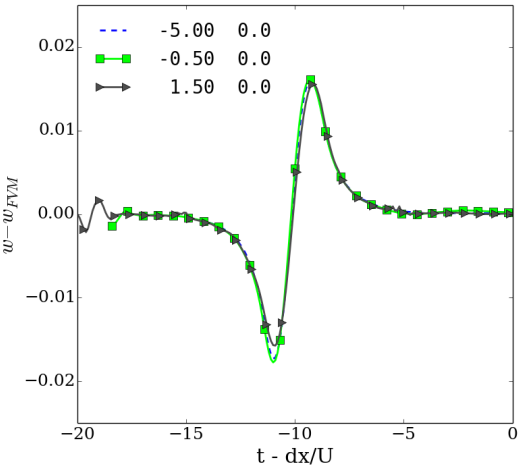


(f) z-velocity, difference to FVM

Figure 11: Comparison of gust induced lift and moment coefficients as well as velocities at different grid locations for $\lambda = 3c$ and Mach = $0.754$

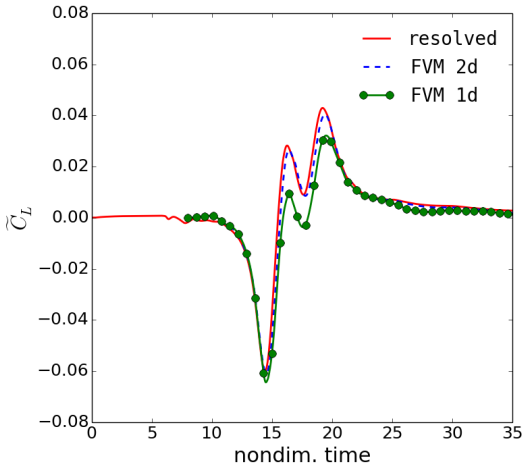


(a) disturbance lift coefficient $\widetilde{C}_L$

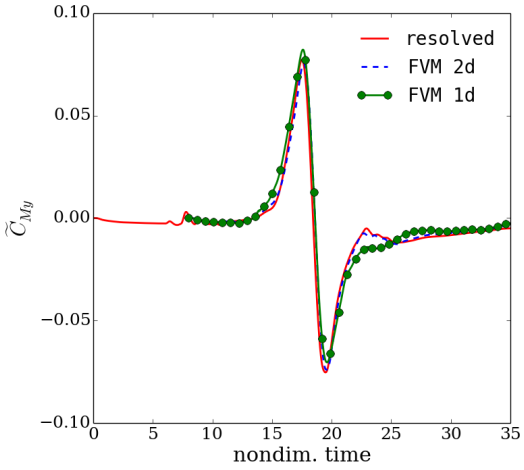


(b) disturbance moment coefficient $\widetilde{C}_M$

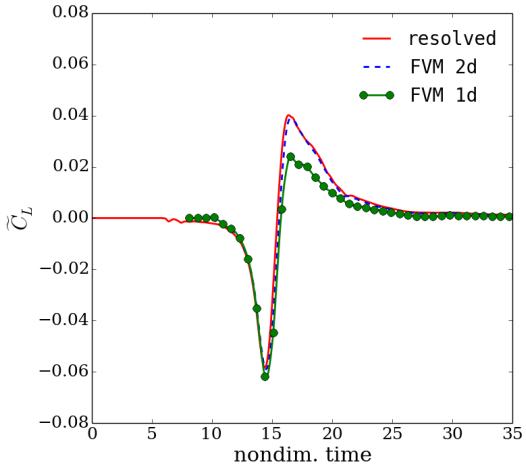


(c) disturbance lift coefficient $\widetilde{C}_L$, wing

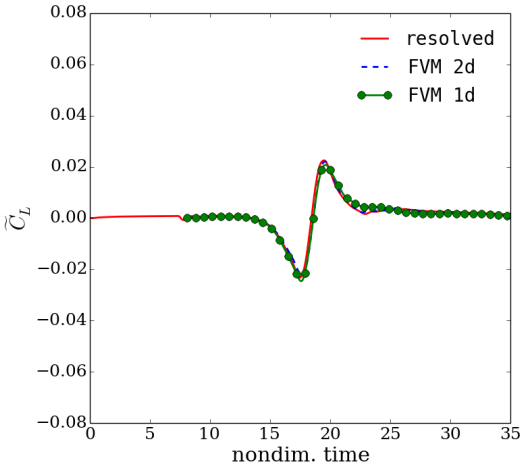


(d) disturbance lift coefficient $\widetilde{C}_L$, HTS

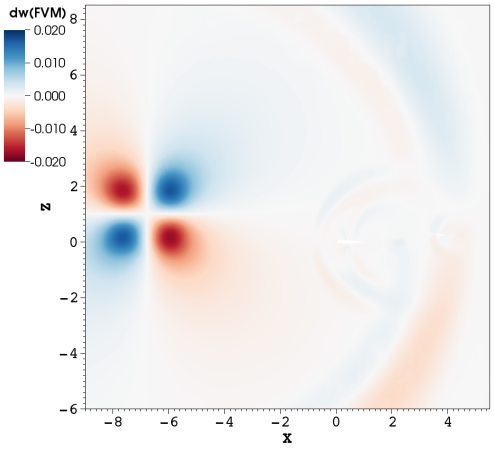


(e) z-velocity, difference to FVM after 8 travelled chords

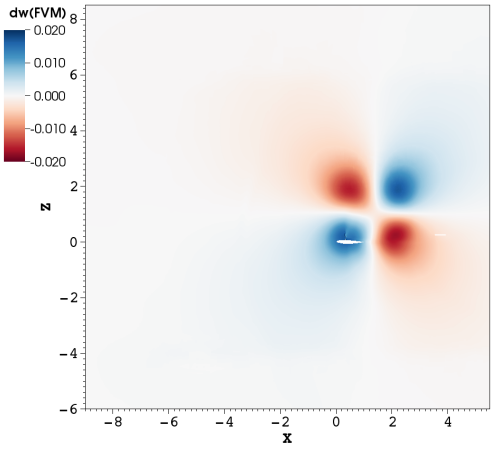


(f) z-velocity, difference to FVM after 16 travelled chords

Figure 12: Comparison of gust induced lift and moment coefficients as well as velocities at different grid locations for the rigid two aerofoil configuration

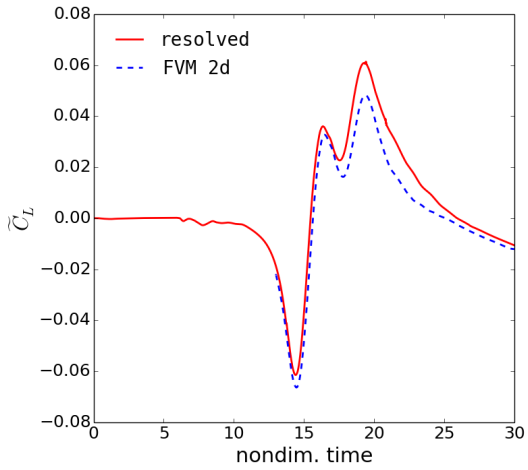


(a) disturbance lift coefficient $\widetilde{C}_L$

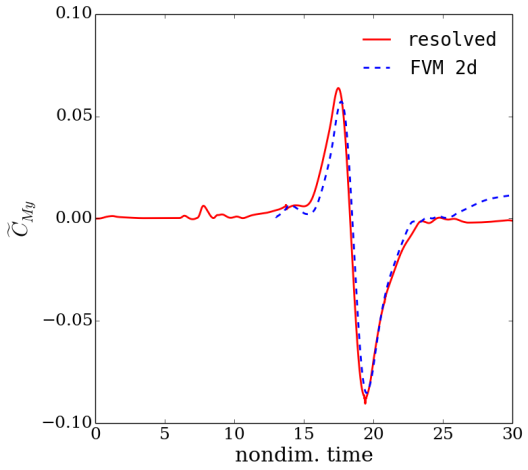


(b) disturbance moment coefficient $\widetilde{C}_M$

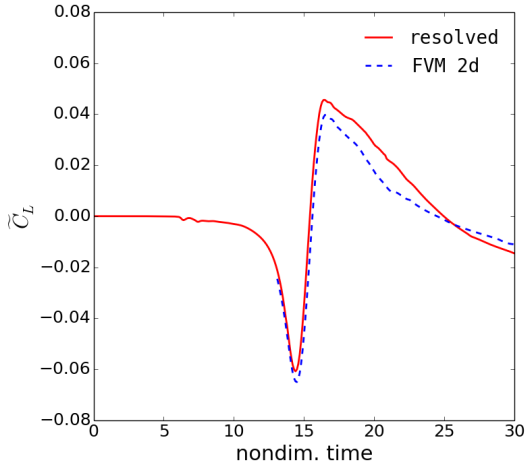


(c) disturbance lift coefficient $\widetilde{C}_L$, wing

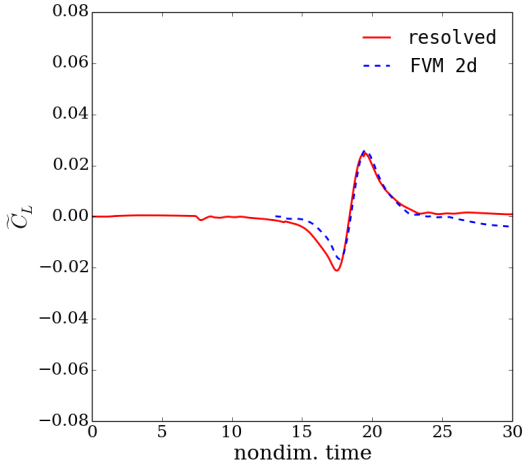


(d) disturbance lift coefficient $\widetilde{C}_L$, HTP

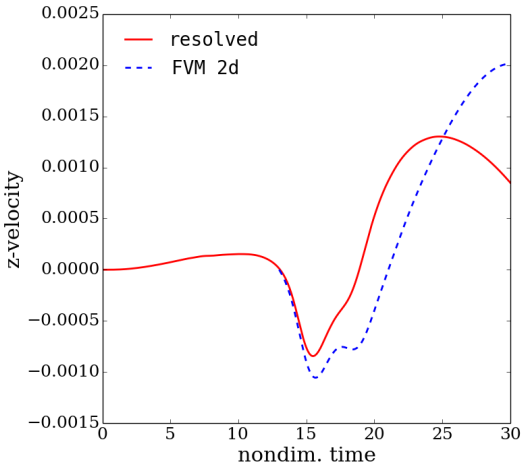


(e) z-velocity of centre of gravity

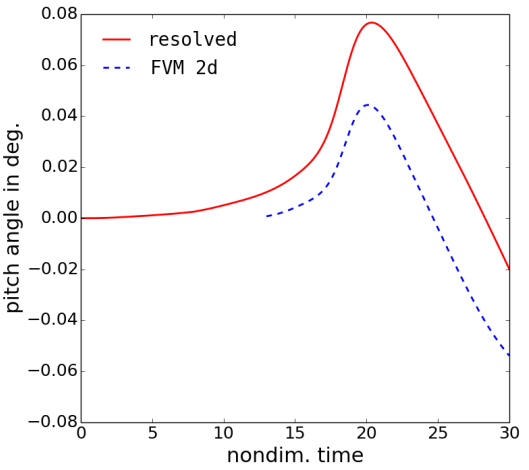


(f) pitch angle

Figure 13: Comparison of gust induced lift and moment coefficients as well as z-translation and pitch angle for the coupled two aerofoil configuration (preliminary)

## 6 REFERENCES


[1] Albano, E. and Rodden, W. P. (1969). A doublet lattice method for calculating lift distribution on oscillating surfaces in subsonic flow. *AIAA Journal*, 2(7), 279–285.

[2] Parameswaran, V. and Baeder, J. D. (1997). Indicial aerodynamics in compressible flow-direct computational fluid dynamic calculations. *Journal of Aircraft*, 34(1), 131–133.

[3] Reimer, L., Ritter, M., Heinrich, R., et al. (2015). CFD-based Gust Load Analysis for a Free-flying Flexible Passenger Aircraft in Comparison to a DLM-based Approach. In *22nd AIAA Computational Fluid Dynamics Conference*. AIAA 2015-2455.

[4] Bekemeyer, P., Thormann, R., and Timme, S. (2016). Rapid Gust Response Simulation of Large Civil Aircraft using Computational Fluid Dynamics. In *Royal Aeronautical Society, Applied Aerodynamics Conference*. AAC 2016-O1.

[5] Heinrich, R. and Reimer, L. (2013). Comparison of Different Approaches for Gust Modeling in the CFD Code TAU. In *International Forum on Aeroelasticity & Structural Dynamics*. IFASD 2013-36B.

[6] Wales, C., Jones, D., and Gaitonde, A. (2014). Prescribed Velocity Method for Simulation of Aerofoil Gust Responses. *Journal of Aircraft*, 52(1), 64–76.

[7] Huntley, S. J., Jones, D., and Gaitonde, A. (2016). 2D and 3D gust response using a prescribed velocity method in viscous flows. In *46th AIAA Fluid Dynamics Conference, AIAA Aviation*. AIAA 2016-4259.

[8] Houbolt, J. C. (1973). Atmospheric Turbulence. *AIAA Journal*, 11(4), 421–473.

[9] Kennett, D. J., Timme, S., Angulo, J., et al. (2013). An Implicit Meshless Method for Application in Computational Fluid Dynamics. *International Journal for Numerical Methods in Fluids*, 71(8), 1007–1028.

[10] Kennett, D. J., Timme, S., Angulo, J., et al. (2012). Semi-Meshless Stencil Selection for Anisotropic Point Distributions. *International Journal of Computational Fluid Dynamics*, 26(9-10), 463–487.

[11] Spalart, P. R. and Allmaras, S. R. (1994). A One-Equation Turbulence Model for Aerodynamic Flows. *Recherche Aerospatiale*, 1, 5–21.

[12] Osher, S. and Solomon, F. (1982). Upwind Difference Schemes for Hyperbolic Systems of Conservation Laws. *Mathematics of Computation*, 38, 339–374.

[13] Saad, Y. (2003). *Iterative Methods for Sparse Linear Systems*. Philadelphia, PA: Society for Industrial and Applied Mathematics, 2nd ed. ISBN 0898715342.

[14] Whitfield, D. L. and Janus, J. M. (1984). Three-Dimensional Unsteady Euler Equations Solution Using Flux Vector Splitting. In *17th Fluid Dynamics, Plasma Dynamics, and Lasers Conference*. AIAA 1984-1552.

[15] Broyden, C. (1965). A class of methods for solving nonlinear simultaneous equations. *Mathematics of Computation*, 19, 577–593.

[16] de Boer, A., van der Schoot M.S., and Bijl, H. (2007). Mesh deformation based on radial basis function interpolation. *Computers and Structures*, 85(11-14), 784–795.

[17] Wright, J. and Cooper, J. (2007). *Introduction to aircraft aeroelasticity and loads*. Wiley.

[18] Cook, M. (2007). *Flight Dynamics Principles*. Elsevier.